JOURNAL OF GEOPHYSICAL RESEARCH, VOL. 104, NO. C6, PAGES 13,467–13,477, JUNE 15, 1999

Experiments on mixing due to internal solitary waves breaking on uniform slopes

H. Michallet[1] and G. N. Ivey

Centre for Water Research, University of Western Australia, Nedlands, Western Australia

Abstract. The shoaling and breaking of an internal solitary wave of depression on a uniform slope were studied experimentally. The waves were generated with as large an amplitude as possible while minimizing mixing at the generation site, thus maximizing the amount of energy propagating onto the slope in the experiment. Various bottom slopes, fluid layer thickness ratios, and density ratios were investigated. The mechanism leading to breaking was examined with flow visualization and particle image velocimetry. Since the layer thickness ratio primarily controls the length (L_W) of the solitary wave (for a given amplitude a), it is found that the ratio of L_W and the characteristic length of the slope L_S determines the amount of energy reflected from the slope. The mixing efficiency of the breaking event, defined as the ratio of the increase of potential energy divided by the amount of wave energy lost at the slope, peaks at a maximum of 25% when $L_W/L_S = 0.5$, with a decrease in efficiency for points on either side of this peak value.

1. Introduction

Long internal waves, primarily generated by tides in the ocean, propagate on the thermocline into the continental margins and coastal zones [*Ostrovsky and Stepanyants*, 1989; *Lamb*, 1994]. In lakes, such waves are generated in response to strong wind events [e.g., *Stevens et al.*, 1996] and are an important means of energy transfer from large scales down to small [e.g., *Saggio and Imberger*, 1998]. *Michallet and Barthélemy* [1998] discussed the existence of solitary internal waves characterized in terms of their amplitudes and of the depth of the thermocline. One can define a large wave when its crest, or trough, is close to the critical level, located at approximately middepth. While the dynamics of such large-amplitudes waves is well known when they propagate in a fluid of constant depth, the dynamics when they propagate into shelving and shoaling regions remains poorly understood. The mechanisms of breaking of internal waves on sloping boundaries and the resulting localized mixing are important in understanding the transport of sediments, nutrients, and other chemical or biological elements in stratified bodies [*Imberger*, 1998].

Numerous studies have been carried out on the breaking of periodic internal waves on sloping bottoms [e.g., *Wallace and Wilkinson*, 1988; *Ivey and Nokes*, 1989; *Taylor*, 1993; *De Silva et al.*, 1997], while comparatively few studies have examined solitary waves. *Kao et al.* [1985] performed laboratory experiments to examine the propagation of internal solitary waves on a slope and shelf geometry. In runs where the amplitude of the wave was sufficiently large, they noticed breaking. The back side of the wave became unstable to an apparent shear instability, and turbulent mixing occurred. *Wessels and Hutter* [1996] experimentally studied the interaction of long internal waves with a sill and the energy loss caused by the interaction. In all their experiments the horizontal extent of the sill was fixed and of the same order as the characteristic length of the wave. They showed that the ratio of the height of the sill to the thickness of the lower layer was the parameter controlling the amount of transmitted and reflected energy.

Helfrich [1992] performed laboratory experiments to observe the interaction of a solitary wave of depression with a sloping bottom. He described the fission of the incoming wave of depression into several solitary-like waves of elevation (or boluses) and the subsequent evolution of the boluses on the slope. The incoming solitary waves were all of relatively small amplitude, compared with those studied by *Michallet and Barthelemy* [1998], for example, and the slope was small ($\alpha < 4°$). Only one configuration of layer thickness ratio was considered by *Helfrich* [1992]. He estimated that the energy of the reflected waves was less than 25% of the incident wave energy and that somewhere between 5% and 25% of the available energy was converted by vertical mixing to an irreversible increase in potential energy. Helfrich was unable to discern any dependence of the mixing ef-

[1]Now at Laboratoire des Ecoulements Géophysiques et Industriels (Université Joseph Fourier, Institut National Polytechnique de Grenoble, CNRS), Grenoble, France.

Paper number 1999JC900037.
0148-0227/99/1999JC900037$09.00

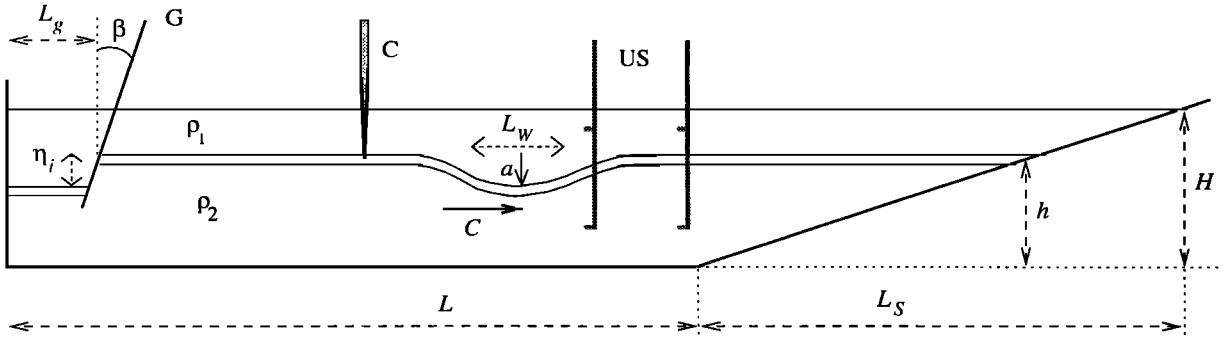

Figure 1. Schematic diagram and notation. "C" and "US" stand for conductivity and ultrasonic probes. "G" is the gate-type wave-generator. Shown on the left is an initial condition, and in the middle is shown the solitary wave resulting from the removal of the gate.

ficiency on external parameters, such as length of the wave or slope angle, but his observed range of mixing efficiencies was consistent with values obtained by *Ivey and Nokes* [1989] in their study of critical internal periodic waves intersecting the sloping bottom in a continuously stratified fluid.

The aim of the present study is thus to determine the amount of energy in the incident wave that is either reflected from the slope or lost to mixing and how this distribution of input energy varies with the experimental parameters: the slope, the layer thickness ratio, and the density ratio. We extend earlier work by considering for the first time waves of large amplitude and also by considering the effect of varying the bottom slope up to steep slopes with angles of 12°. The paper is organized in the following manner: The experimental facility is described in section 2. Section 3 is devoted to a description of the shoaling/breaking event. We examine the amount of energy reflected from the slope after wave breaking in section 4. In section 5 the mixing efficiency is estimated, and we conclude in section 6 by comparing the experimental conditions with field observations.

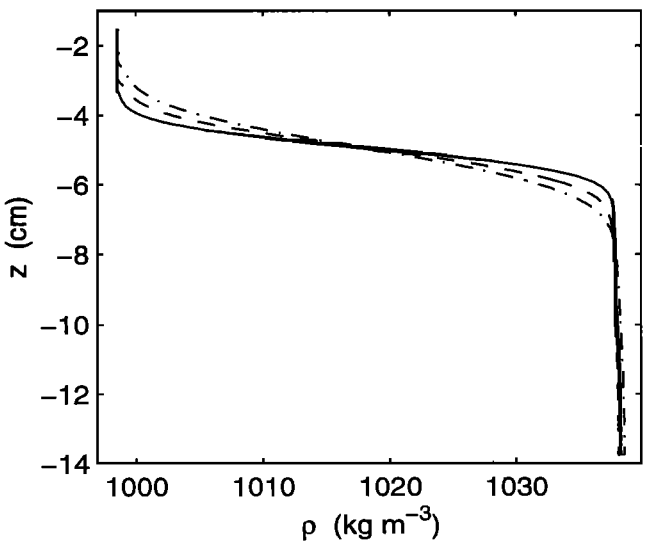

Figure 2. Density profiles, experiment 7. Solid line shows initial stratification; dashed line indicates after three runs; and dashed-dotted line indicates after five more runs.

2. Experimental Facility

The experimental setup is represented schematically in Figure 1. The Perspex and metal frame flume had a width of 25 cm and a depth of 20 cm. Its length before the start of the slope was $L = 2.3$ m. We investigated three different slopes: $s = 0.069$, 0.169, and 0.214 (angles of 4°, 9°6, and 12°1). In operation, the flume was filled with fresh water to a desired depth, and then a brine solution was slowly injected beneath the lighter fresh water until the total water depth was $H = 15$ cm. The layer thickness ratio was varied in the range $0.60 \leq h/H \leq 0.91$, where the depth scale h is the distance separating the midhalocline from the bottom (see Figure 1). The thickness of the halocline between the two layers was approximately 1-2 cm at the start of the experiments and tended to become larger after each run, as determined from density profiles (e.g., Figure 2). The density ratio (ρ_2/ρ_1) ranged from 1.012 to 1.044.

Density profiles were obtained by traversing a (Precision Measurement Equipment) four-electrode microconductivity probe over the depth and converting conductivity to density by calibration against an Anton Paar digital densimeter; the overall resolution is better than 0.1 kg/m^3 (see also section 5). Profiles were taken when the fluid was quiescent, at a vertical traverse speed of 2 cm/s while sampling at 50 Hz. The procedure was then to repeat a given release experiment or run several times (at least three) for the same wave (i.e., the same initial condition) so that the increase of potential energy was large enough to be estimated with good precision (see section 5). Some of the experiments were divided into two set of runs, and the increase in potential energy was estimated after each set. A complete summary of all the experimental conditions is provided in Table 1.

Table 1. Summary of Experimental Conditions

Experiment	Number of Runs	Symbol	s	ρ_2/ρ_1	h/H	a, cm	L_W, cm	C, cm/s	E_0, J/m
1	6	right-pointing triangles	∞	1.039	0.66	2.2	54	10.6	0.052
2	8	left-pointing triangles	∞	1.040	0.82	2.9	26	10.3	0.046
3	3 – 6	open circles	0.069	1.020	0.65	1.5 – 2.2	54	7.9	0.017 – 0.033
4	7	open circles	0.069	1.020	0.78	3.0	30	7.7	0.045
5	6	solid circles	0.069	1.040	0.70	2.0	32	10.3	0.041
6	5	solid circles	0.069	1.039	0.90	2.4	15	9.8	0.026
7	3 – 5	solid squares	0.169	1.040	0.67	2.0	46	10.7	0.045
8	3 – 3	solid squares	0.169	1.040	0.83	2.8	24	10.2	0.054 – 0.052
9	3	solid squares	0.169	1.040	0.91	3.0	17	9.8	0.032
10	4 – 4	open diamonds	0.214	1.013	0.63	2.2	52	6.1	0.018
11	4 – 6	open diamonds	0.214	1.013	0.71	1.9 – 2.5	40	6.0	0.010 – 0.018
12	4 – 6	open diamonds	0.214	1.012	0.84	2.5 – 3.1	24	5.6	0.010 – 0.015
13	4 – 4	solid diamonds	0.214	1.044	0.60	1.6 – 2.0	56	10.8	0.037 – 0.056
14	5 – 6	solid diamonds	0.214	1.046	0.67	1.9 – 2.2	46	11.0	0.043 – 0.060
15	5	solid diamonds	0.214	1.047	0.77	2.7	32	10.8	0.067
16	4	solid diamonds	0.214	1.048	0.80	2.8	30	10.6	0.066

Here $s = H/L_S$ is the slope, ρ_2 and ρ_1 are the lower and upper densities, and h and H are the interface and surface levels at rest ($H = 15$ cm for all experiments). The wave amplitude a, the wave length L_W (equation (1)), the phase velocity C, and the energy E_0 (equation (2)) are averaged values (over a same set of runs) estimated at the base of the slope.

The procedure to generate a solitary wave was as follows. A watertight, manually movable gate was located near the upstream end of the tank (see Figure 1). Fresh water was pumped with a small pump from the downstream side of the gate and reintroduced on the other side, thus lowering the halocline level behind the gate compared with the main part of the flume. The gate was lifted to initiate a run. The distance L_g between the wall and the gate was adjusted in order to minimize the production of trailing waves and ranged from 15 to 30 cm, depending on the thickness ratio. Such a gate-type wavemaker is able to produce large-amplitude solitary waves while minimizing the generation of barotropic perturbations [*Michallet and Barthélemy*, 1998]. Experience has shown that if the gate was slightly tilted (relative to the vertical at an angle $\beta \simeq 30°$), the mixing was minimized when the wave was formed (the initial volume of released fluid was thus close to the final wave shape). The distance L_g, the angle β, and the amount of fresh water transferred were precisely known, enabling us both to estimate the amount of energy initially put into the system and to reproduce the initial wave in different runs.

Ultrasonic probes were used to measure the interface vertical displacement of the wave propagating along the density interface. An ultrasonic pulse is emitted from one piezoelectric ceramic and received by a second identical sensor 10 cm away. At first order, the speed of sound is linearly proportional to the density of the fluid it encounters. The probes provide time series recordings of displacements of the isopycnals in the density interface, under the assumption that all the isopycnals are symmetrically displaced by the propagating internal wave. Careful visual observation of the wave when propagating at constant depth indicated that this assumption is acceptable. The minimum measurable displacement is about 0.1 mm. Note that the probing device was not designed to measure mode-two vertical waves in the present configuration but the gate-type wavemaker was designed to generate only first-mode waves, and indeed no second-mode waves were observed. Moreover, since the propagation speed of mode-two waves is a lot smaller than for mode-one waves, we were confident that the probe response was dominated by first-mode waves. At least two probes at different horizontal locations were used in order to estimate the wave phase velocity.

In order to quantify the velocity field, a particle image velocimetry (PIV) technique was used. Particles were sieved to create a curtain of aluminum particles illuminated by a white light sheet about 0.5 cm thick. Images from a charge-coupled device (CCD) camera were recorded onto super VHS video tape and digitized (768 × 572 pixels) after passing through an eight-bit analog-to-digital (A/D) converter. The velocity field was calculated with two consecutive frames using a cross-correlation technique [*Stevens and Coates*, 1994], where the time interval between two images was set to 0.08 s. Velocities are resolved with an accuracy of about 0.25 cm/s and the spatial resolution in the flow field is about 0.1 cm.

3. Description of Wave Breaking

The shoaling of the wave on the slope for a typical run is shown in Figure 3. The wave is traveling from left

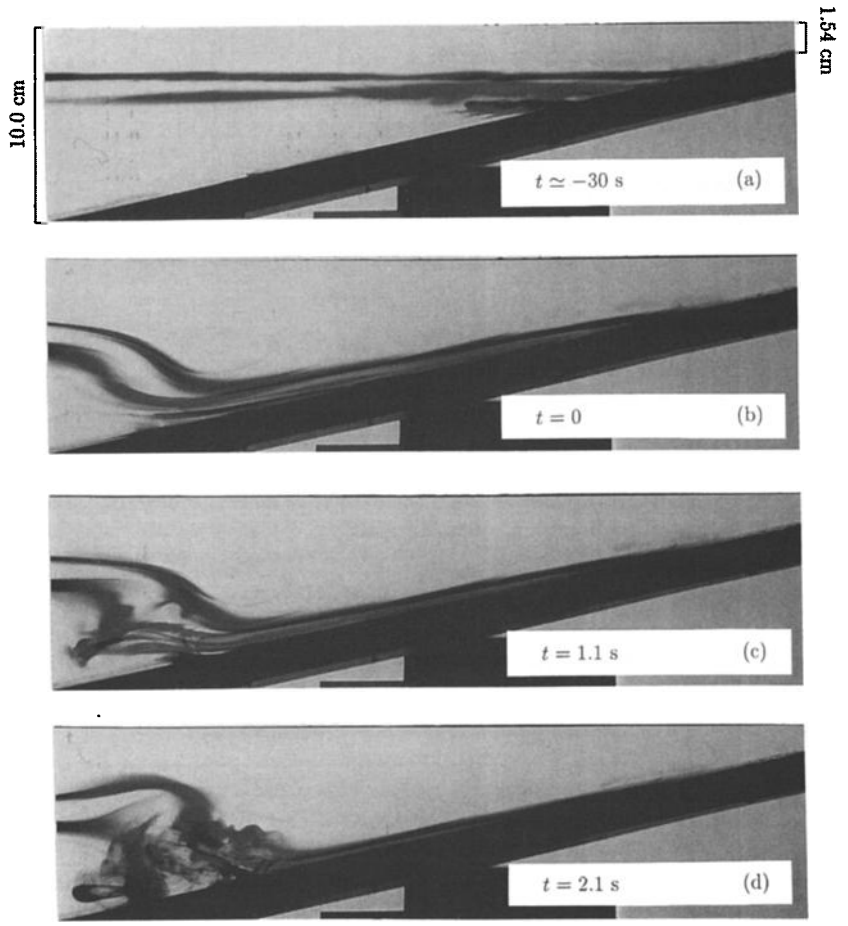

Figure 3. Sequence of photographs showing the shoaling internal wave (experiment 15; see Table 1).

to right in the upslope direction. The first frame (Figure 3a) shows the medium at rest, where dye has been injected prior to the experiment. The green-dyed fluid (G) is slightly heavier than the fresh water in the upper layer ($\rho_G = 1.01 \times \rho_1$), the red dye ($R$) is of intermediate density ($\rho_R = 1.03 \times \rho_1$), and the blue dye ($B$) is of the density of the lower layer ($\rho_B = \rho_2 = 1.047 \times \rho_1$). At the early stage, the front side of the incoming wave of depression becomes parallel to the slope, while the back side is steepening (Figure 3b). The interface is very thin at the front but is thickening at the back. Blue dye is then drawn to the left and away from the slope and then down (Figure 3c). The first three-dimensional motion indicative of a growing instability appears at this stage: Some red dye is observed to be located below heavier blue dye. Note that the green isopycnal is the less disturbed isopycnal. At the next stage (Figure 3d) the individual dye layers continue to wrap around one another as the instability grows, until, by Figure 3e, the individual dye layers have been disrupted and appear to have formed for the first time a core of mixed fluid. Note that upslope of this core of mixed fluid or bolus [*Helfrich*, 1992] there is only relatively light fluid, while behind the bolus the green isopycnal elevated in Figure 3d collapses in Figure 3e and mixes with the denser isopycnals. The bolus, dragging heavy blue fluid up and green light fluid down at its back, propagates onshore. In Figure 3g, its propagation is then similar to a density current as studied, for example, by *Wood and Simpson* [1984]. Note that there still appears to be some active turbulence in Figure 3f and even Figure 3g, which shows nearly horizontal striations typical of the decay of turbulent mixing events in stratified fluids [*Pearson and Linden*, 1983]. The bolus reaches its maximum run-up position in the last frame, Figure 3h. The diffusion of dyes due to mixing is evident in the breaking region, defined by the distance L_M separating the position of appearance of the first instabilities till the point where the bolus dissipates. Note that L_M is of the order of half the total length of the slope L_S.

Velocity fields obtained with the PIV technique are overlain on the raw pictures, and the resulting images for two typical runs are shown in Figures 4 and 5. The particles used were not perfectly uniform in size: The strong density gradients tended to create sheets and lines of particle concentrations, and once stretched by the incoming wave, these lines show roughly the distortion of the isopycnals. A dark line may thus represent the wave shape, as, for instance, in Figure 4a. The flow associated with the incoming wave is characterized by a

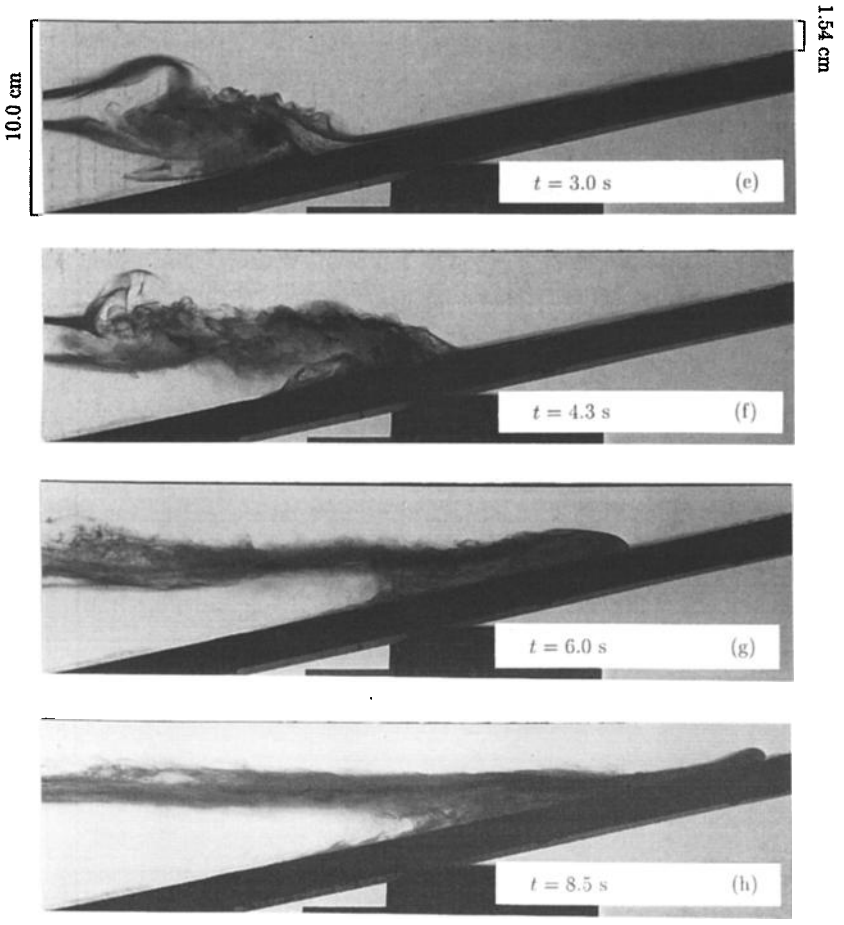

Figure 3. (continued)

shear at the interface: a flow up the slope in the upper layer and down the slope in the lower layer. The first distortion to this relatively symmetric flow is localized at the back of the wave, close to the bottom. Indeed, in Figure 4a, while the velocity field is still characterized by velocities down the slope under the wave trough (bottom right), some upslope velocities are measured behind the wave (bottom left, for $x < 35$ cm). These velocities correspond to the separation of the lower-layer flow from the bottom, likely induced by an adverse pressure gradient. As the wave shoals, the pressure gradient is increasing, enhancing the vertical velocities at the back of the wave. Note that the back of the wave becomes potentially unstable (velocity vectors cross the apparent isopycnals perpendicularly at $x \simeq 35$ cm and $y \simeq -4$ cm). Heavy fluid is lifted upward into a region of less dense fluid. This contributes to the creation of a vortex behind the wave (Figure 4b), which in turn brings light particles down behind the wave (this stage corresponds to Figure 3d). The vortex reaches its maximum size in Figure 4c, corresponding to the formation of the bolus as shown in Figure 3e. The velocity field shown in Figure 5 corresponds to the upslope propagation of the bolus shown in Figures 3f and 3g. We note a strong flow up the slope close to the bottom and a flow offshore in the upper layer, corresponding to the reflection of the first-mode long wave, and there are signs of strong turbulent activity at the interface (for $26 < x < 32$).

Rather than a shear instability (as suggested by *Kao et al.* [1985]), the first sign of breaking seems to be a gravitational instability, following the separation of the flow in the lower layer. This was suggested by *Wallace and Wilkinson* [1988] to explain the breaking of periodical waves and the formation of similar bolus. This behavior was also observed for mixing events driven by wave-wave interactions [*Teoh et al.*, 1997]. Note also that the main part of the mixing occurs in the lower layer [*Wood and Simpson*, 1984]. The process described above is similar to what is observed for a weaker slope, except that in the latter case the breaking is less intense but occurs over a longer distance. *Helfrich* [1992] has observed up to 10 boluses, for example, resulting from the breaking of a solitary wave on a very weak slope ($s = 0.034$). An extrapolation of his results suggests that one or two boluses would emerge for $s \geq 0.169$. For $s = 0.214$ we observed one main bolus and a complicated wake from which no other boluses seemed to emerge (see Figures 3g and 3h).

4. Energy Budget

The time series recordings of four different runs are presented in Figure 6, where in all cases the traces come from an ultrasonic probe located at some distance from

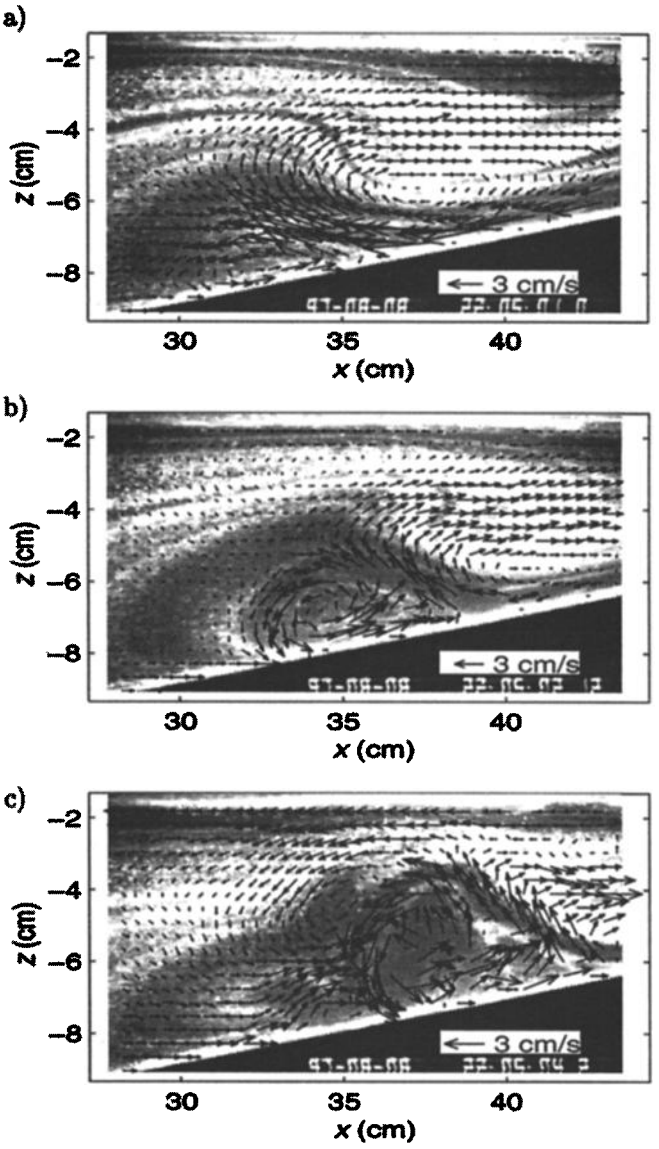

Figure 4. Velocity fields overlain on the photographs of the particle-seeded flow (experiment 12; see Table 1). The start of the slope is at $x = 0$, and the free surface is at $z = 0$. Figures 4b and 4c are taken 1.1 and 2.5 s after Figure 4a.

the start of the slope. We have offset the time traces so that the maximum disturbance of the interface passes the observer at the same instant and the variations in steepness of the incoming waves can thus be readily compared. Each trace shows a similar evolution: some very small initial perturbations, followed by the large depression due to the solitary wave itself and then a lee region with a combination of an oscillatory tail and some evidence for a shelf region [e.g., *Knickerbocker and Newell*, 1980], followed finally at later time by a signal associated with the portion of the incident wave that is reflected from the slope and moves past the sensor as it moves offshore. The small initial perturbations the sensor as it moves offshore. The small initial perturbations are barotropic disturbances associated with the removal of the gate and propagate rapidly ahead of the internal wave, but the remaining portion of the trace is associated with the internal wave.

The layer thickness ratio h/H determines both the phase velocity and the steepness of the wave. Experiments 5 and 6 shown in Figure 6a were both performed for the same bottom slope and density ratio (Table 1). We note that for experiment 6 in Figure 6a the incoming wave is steep with a relatively narrow pulse, while the reflected wave, recorded for $90 < t < 120$ s, is of very small amplitude and clearly most of the wave energy has been dissipated on the slope. On the other hand, the incoming wave in experiment 5 was not as steep, with a broader pulse, and the corresponding reflected wave, recorded for $50 < t < 90$ s, is similar to a very long wave and there appear to be greater amounts of energy reflected from the slope than in experiment 6. A steeper bottom slope case is shown in Figure 6b, and in this case the reflected waves in the two experiments (10 and 12), and hence the reflected energy, are a lot larger in amplitude than for the experiments in Figure 6a. The time series record thus suggests that the amount of energy that is dissipated on the slope is dependent on the characteristic length scales of both the incoming wave and the slope.

The time series from the probes provided the wave characteristics, namely, the amplitude a (i.e., the max-

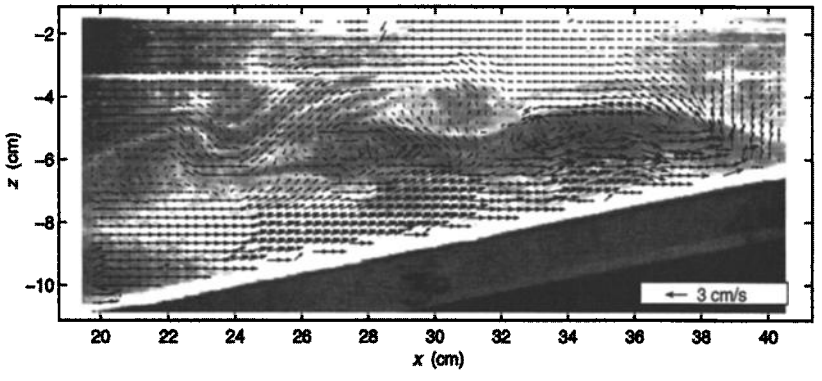

Figure 5. Same as Figure 4, but for experiment 11.

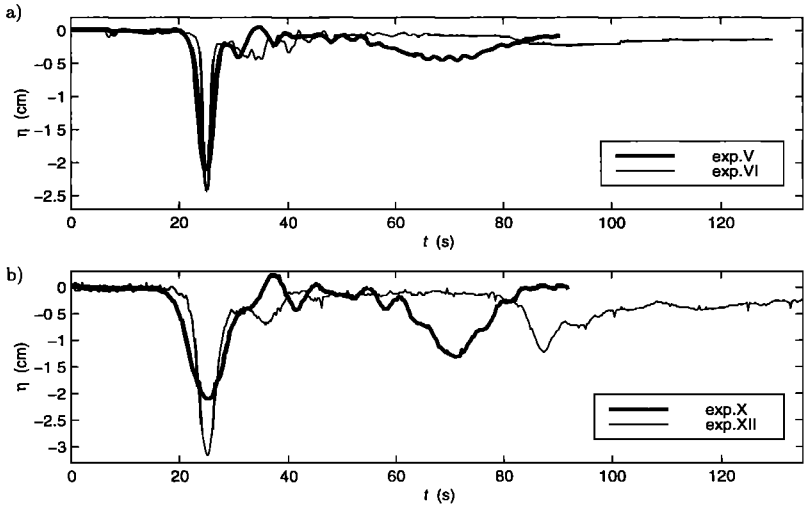

Figure 6. Time series of the interface displacement. The probe was 40.4 cm (experiments 5 and 6) and 99.8 cm (experiments 10 and 12) away from the start of the slope.

imum displacement of the isopycnals), the wave phase velocity C, and a characteristic length L_W defined as [*Koop and Butler*, 1981]

$$L_W = \frac{1}{a}\int_{-\infty}^{\infty} \eta(x)\, dx \qquad (1)$$

$$L_W \simeq \frac{C}{a}\int_{t_0}^{t_1} \eta(t)\, dt.$$

The total energy of each long wave is estimated as [e.g., *Bogucki and Garrett*, 1993]

$$E = C\, g\, \Delta\rho \int_{t_0}^{t_1} \eta^2(t)\, dt \qquad (2)$$

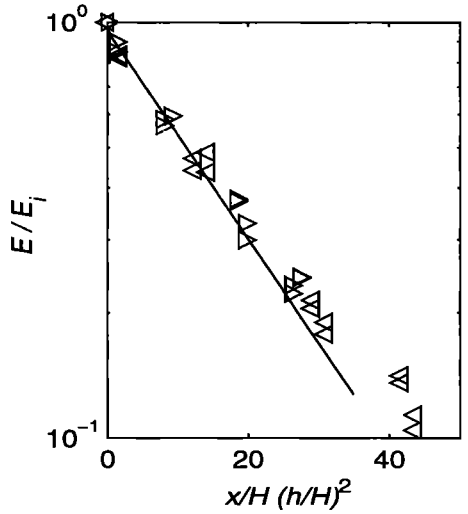

Figure 7. Decrease of wave energy against the traveled distance for the wave propagating at constant depth: four runs of reference experiments 1 (right-pointing triangles) and 2 (left-pointing triangles). One flume length corresponds to $x/H\ (h/H)^2 \simeq 10$.

where $\eta(t)$ is the interface displacement, $g = 9.81$ m/s^2, $\Delta\rho = \rho_2 - \rho_1$, and t_0 and t_1 are estimates such that $\eta(t_0) \simeq \eta(t_1) \simeq 0$. For instance, in Figure 6 for experiment 5, $t_0 = 18$ s and $t_1 = 30$ s are chosen to compute the energy of the incoming wave E_0; $t_0 = 47$ s and $t_1 = 90$ s are chosen to compute the energy of the wave after breaking E_R.

Two experiments have been performed without the slope (experiments 1 and 2). The waves were free to reflect on the vertical walls at each end of the tank, and these runs allowed us to estimate the dissipation of the solitary wave during its propagation in a fluid of constant depth. Many authors have studied the viscous dissipation of internal solitary waves [e.g., *Leone et al.*, 1982; *Maurer et al.*, 1996], and it was useful to experimentally estimate the energy lost in our tank. In Figure 7 we plot the nondimensional wave energy against the nondimensional distance weighted by the layer thickness ratio. This nondimensionalization allows us to plot a single fitted line for the data for two different thickness ratios for the case when the wave has traveled less than two flume lengths. We were therefore able to estimate the energy (and in the same way a and L_W) at the start of the slope by measuring the waves farther offshore, where the corresponding recordings well differentiate the incoming wave from the reflected wave (a similar procedure was used by *Wessels and Hutter* [1996]). We note from Figure 7 that in our experiments, the wave loses approximately 40% of its initial energy during its first flume-length travel.

The accuracy of the estimates of E_0 and E_R depends on the choice in (2) of t_0 and particularly t_1 accounting for the energy in the lee of the main depression. We have computed E_0 and E_R for an interval $(t_1 - t_0)$ 10% longer or smaller than the nominal one (i.e., than the one which seemed the most appropriate). This test gave an uncertainty in E_R/E_0 of $\pm 5\%$ and an uncertainty in

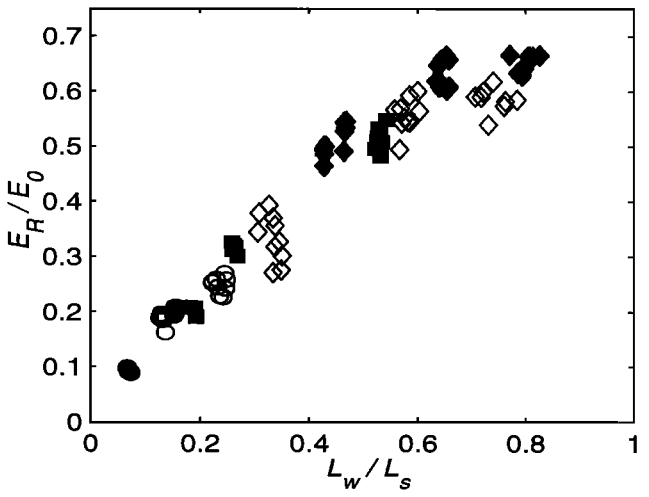

Figure 8. Rate of energy lost on the slope against characteristic length ratio (see list of symbols in Table 1).

L_W of ±3%. In fact, during the experiment, the interface is thickening and thus the waves do not propagate in exactly the same medium resulting in a slight decrease in the phase velocity of the waves. These various effects conspire, and for the entire experiment we estimate that the overall accuracy of the estimate of L_W is about 5%, is 8% for incident energy E_0, and is 10% for reflected energy E_R.

These accuracies correspond well with the observed scattering of the data in Figure 8, where we plot the ratio of reflected to incident energy E_R/E_0 against L_W/L_S, the length scale ratio suggested by the observations described above. The solid circles (for which $\rho_2/\rho_1 \geq 1.039$) are generally less scattered than the open circles ($\rho_2/\rho_1 \leq 1.020$). The closer to 1 the density ratio is, the smaller the amount of energy initially involved in the experiment, and the relative errors ascribed to the latter circles are therefore slightly larger. Moreover, we have noted in our experiments a tendency for the ratio E_R/E_0 to slightly decrease with the thickening interface from run to run (see, for instance, the group of open diamonds for $0.3 < L_W/L_S < 0.35$ in Figure 8), but, given the accuracies involved, the main result from Figure 8 is the progressive increase of E_R/E_0 with L_W/L_S.

In all cases considered in this study, L_W is at least twice the total depth H (see Table 1). The wave therefore has to "adapt" its shape to the new environment as its leading edge encounters the slope. In the limit of a very shallow slope, L_S tends toward infinity, and therefore L_W/L_S tends toward zero. We can expect in this limit that all the wave energy will be dissipated by viscous effects before it reaches an eventual breaking zone and E_R/E_0 tends to zero. When L_W/L_S is increasing, Figure 8 shows that the ratio E_R/E_0 initially increases almost linearly, independent of the density ratio. Beyond $L_W/L_S \simeq 0.5$, however, the rate of increase appears to slow and E_R/E_0 asymptotically approaches the limiting value of $E_R/E_0 = 1$ expected for large L_W/L_S (i.e., when L_S tends to zero and the bottom slope increases to the case of a vertical wall). We suggest that above $L_W/L_S \simeq 0.5$ the timescale of interaction between the wave and the slope starts to become too short for much energy loss to occur. This point will be discussed in the next section in light of the estimations of the increase of the potential energy of the fluid due to mixing.

5. Mixing Efficiency

A given experiment involved multiple runs, and the amount of mixing was computed by comparing the initial and final density profiles obtained from the conductivity probe vertical traverses. Because an entire experiment could take several hours, any tendency for drift in the conductivity probes had to be corrected in order to obtain accurate estimates of the potential energy changes in the fluid column. Any drift effects were minimized by checking that the total mass M was conserved, where M is defined as

$$M = \int_{-H}^{0} \rho B dz \tag{3}$$

where $B(z) = L + Ls\,(1 + z/H)$ is the horizontal extent of the trapezoidal region at a depth z. The typical accuracy in the calculation of M was ±0.01%. The potential energy was then computed as

$$E_p = \int_{-H}^{0} \rho g z B dz\,. \tag{4}$$

To estimate the accuracy in the estimates of E_p, we proceeded as described below. A typical density profile $\rho(z)$ was used. Vertical and horizontal drifts were simulated on the artificially noised profile:

$$\rho'(z) = \rho(z + c_1) + c_2 z + c_3(z)\,, \tag{5}$$

with $c_1 = 0.1$ mm (which corresponds to the uncertainty in the starting position of the profiler), $c_2 = 5$ kg/m^4 (typical of the error we estimate from the mass conservation check), and $c_3(z)$ is a white noise fluctuating between -0.1 and 0.1 kg/m^3 (which corresponds to the probe resolution). Comparison of E_p computed from the two profiles, one based on $\rho(z)$ and one based on $\rho'(z)$, indicated that the typical error in the calculation of E_p from (4) was ±0.001 J/m which represents from 2% to 30% of the increase of potential energy we measured in our experiments.

By comparison, *Helfrich* [1992] made estimates of the increase in potential energy using a different technique, one involving dropping a gate above the sloping region after the incident wave has come through. This prevents the mixed fluid on the slope from propagating offshore. In our facility we felt that such a procedure was possibly a source of additional error due to the slight but nevertheless significant displacement of the final stable

density profile, relative to the initial profile, that can occur. A slight modification of the mean interface level would induce an error in the estimation of the mass (equation (3)), and consequently in the estimation of the potential energy (equation (4)). The main drawback to not inserting a gate above the sloping region is that the wave, once reflected by the wall at the generation side, shoals a second time on the slope. Even for the strongest slope ($s = 0.214$), however less than 10% of E_R (the energy left after the breaking event) is dissipated during the second shoaling event, which represents less than 7% of E_0 (see Figure 8). Moreover, the fraction of energy dissipated on the slope by viscous effects increases as a decreases [*Helfrich*, 1992]. Therefore the potential contribution to mixing from the second shoaling event was neglected in our analysis.

Another contribution to mixing could be induced by the shear of the interface which characterizes the propagation of the solitary wave. If we refer to *Bogucki and Garrett* [1993, equation (9)], the two lowest values of the soliton-induced Richardson number were approximately 0.4 and 0.6 for experiments 9 and 6, where $h \sim 1.5$ cm at the beginning of the experiments. These values are estimated by considering the soliton amplitude at the early stage of wave propagation. In all cases, their equation (13) was not satisfied (i.e., $a < a_c$, a_c being the minimum amplitude to lower Ri sufficiently to obtain soliton-induced shear mixing), except for experiments 9 and 6. Accordingly, we did not estimate the mixing in these two experiments. For all other runs, critical conditions were never reached because the interface was too thick, except perhaps during shoaling. The interface is effectively very thin at the front of the wave in Figure 3b. Again, though, no Kelvin-Helmoltz or shear instability has been identified when the wave is shoaling (see section 3). If this occurs, this is probably negligible in front of the main source of mixing, that is, the Rayleigh-Taylor or gravitational instability.

The two reference experiments (1 and 2, discussed in section 3) allowed us to estimate that 0.3-0.4% of the total energy put into the initial condition goes into mixing during the generation process, the propagation of the wave at constant depth, and any eventual diffusive effects (note that diffusivity is acting on a lot larger timescale than other sources of mixing and is therefore probably negligible). Correspondingly, about 5% of the increase of the potential energy is thus due to the removal of the gate and the early stage of the wave formation, and this part was removed when estimating ΔE_p.

We first plot ΔE_p nondimensionalized by E_0 against L_W/L_S in Figure 9, which clearly shows a peak in $\Delta E_p/E_0$ near $L_W/L_S \simeq 0.4$, with smaller values of the energy ratio above and below this point. When L_W/L_S is small, viscous effects are relatively strong as the waves propagate up the slope, and the shoaling and breaking of the wave are relatively inefficient in terms of mixing. For $0.3 \leq L_W/L_S \leq 0.5$, a larger part of the incoming energy E_0 is transferred into an increase of the potential energy of the system. However, for $L_W/L_S \geq 0.5$ the trend is clearly that ΔE_p decreases with increasing L_W/L_S. We suggest in this case that the interaction time of the wave with the slope is not long enough for the instabilities to develop completely. Indeed, in the limit of a vertical wall (L_S goes to zero or L_W/L_S goes large), we observed no instability at all.

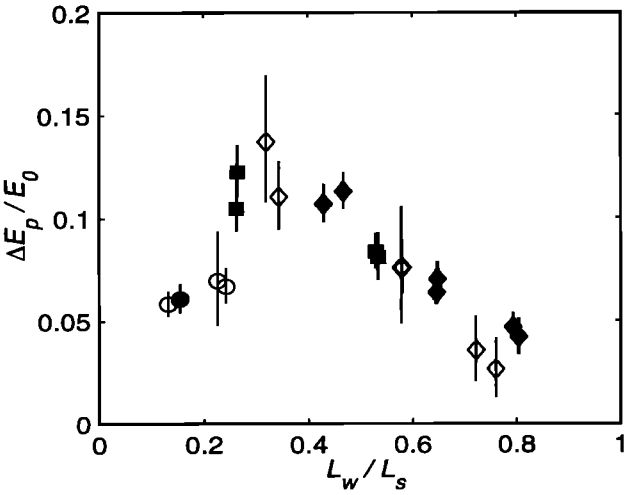

Figure 9. Increase of the potential energy over the incoming wave energy against characteristic length ratio (see list of symbols in Table 1).

We then compute the mixing efficiency, defined as

$$R_f = \frac{\Delta E_p}{E_0 - E_R} \tag{6}$$

$$R_f = \frac{\Delta E_p/E_0}{1 - E_R/E_0} \tag{7}$$

R_f is plotted against L_W/L_S in Figure 10. The variation of mixing efficiency observed in Figure 10 can thus readily be understood in terms of the behaviors plotted in Figure 9, which represents the numerator of (7), and in Figure 8 which is the parameter occurring in the denominator of (7). Error bars are plotted in Figure 10 estimating an accuracy of 10% in the difference $(E_0 - E_R)$ (corresponding to the scattering of the data in Figure 8) and an error of 0.001 J/m in ΔE_p (see above). Indeed, the increase of potential energy is very small even after several breaking events, and the uncertainty in E_R decreases the accuracy of R_f compared with the accuracy of $\Delta E_p/E_0$. The relative accuracy in R_f is therefore about 30%.

The mixing induced by a breaking internal solitary wave is qualitatively very different from the mixing induced by periodical waves, as studied by *Ivey and Nokes* [1989], for instance. In their case the turbulence generated after several wave periods may be considered locally homogeneous and isotropic, which allows the use of turbulent Reynolds or Froude numbers. In our case the breaking event is very localized in time and space and is best described by the length scale ratio L_W/L_S.

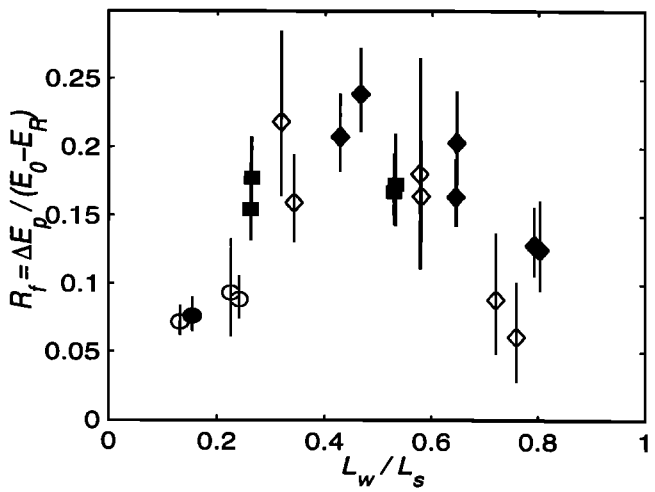

Figure 10. Mixing efficiency against characteristic length ratio (see list of symbols in Table 1).

If the slope is very gentle ($L_W/L_S \to 0$), the wave propagation over the slope approaches that of a wave in fluid of constant depth, viscous losses dominate, the reflected energy naturally tends to zero, and little energy is converted to an increase in potential energy due to mixing. On the other hand, when the slope is very steep ($L_W/L_S \to \infty$), the wave/slope interaction occurs on a very short timescale, the ratio E_R/E_0 goes to 1, and again, little energy is converted to an increase in potential energy due to mixing. There is an intermediate value of $L_W/L_S \simeq 0.5$, where the gravitational instabilities fully develop and the mixing efficiency peaks at a maximum of 25%.

6. Discussion and Conclusions

It is interesting to compare our laboratory results with published field observations, and in Table 2 we summarize data from a number of oceanic and lake sites. We have focused on field observations showing strong evidence of solitary waves of large amplitude propagating in a two-layer configuration with shoaling observed on a sloping boundary. The characteristic length L_W given in Table 2 is estimated from signals presented in the quoted papers. In the ocean the continental slopes are generally weak ($s \ll 0.1$), and consequently L_W/L_S is usually very small. This is the case for the Scotian Shelf (first example in Table 2). The implication is that the mixing induced by the breaking of long internal waves is relatively inefficient on continental margins, of the order of a few percent for individual events. One exception is the case of the Sulu Sea, where $s \simeq 1/11$, implying a mixing efficiency around 10% for the observed solitary waves.

Steep slopes are often encountered in lakes. The case of long narrow lakes (such as those investigated by *Hunkins and Fliegel* [1973], *Thorpe* [1974], and *Stevens et al.* [1996]) is interesting because undular bores are often observed. They are thought to be generated in response to a strong wind event and then to evolve into a set of solitary waves which can shoal and break at one of the sloping ends of the basin. From Table 2 we see that for the four sites listed, $0.2 \leq L_W/L_S \leq 0.3$, implying that the mixing efficiency is quite high at $10\% \leq R_f \leq 18\%$ from Figure 10. The data collected by *Hayami et al.* [1996] exhibit some interesting features. In their Figure 9b a solitary wave approaching the shore is shown. This solitary wave evolves at the front of the surge created by a typhoon. The characteristic length scale ratio L_W/L_S is approximately 0.3, suggesting a mixing efficiency R_f of 18%. If we now consider their Figure 9d, however, when the surge is shoaling, L_W/L_S is then about 0.5, implying a very high mixing efficiency of $R_f \simeq 25\%$ for this particular case. The velocity fields provided by *Hayami et al.* [1996] are not of very high definition but showed amazing similarities to the breaking mechanism described in section 3. One can discern, for instance, a separation of the flow in the lower layer and turbulent activity resulting from breaking.

The description of wave breaking in section 3 concluded that the strong flow offshore in the lower layer separates from the sloping bottom, that gravitational instabilities occurred, and that the net result was the transport of mixed fluid off the slope. Indeed, this mechanism contributes to flush heavy fluid down and off the slope. Observations after all motion has ceased have shown that particles initially located in the breaking region are spread very far offshore. In the run shown in Figure 3, for example, the mixed fluid which has been

Table 2. Summary of Field Conditions

Location	Reference	$s = H/L_S$	h, m	H, m	a, m	L_W, m	L_W/L_S	R_f
Scotian Shelf	*Sandstrom and Elliott* [1984]	1/200	100	150	30	1100	0.05	3%
Sulu Sea	*Apel et al.* [1985]	1/11	1400	1500	30	3000	0.2	10%
Loch Ness	*Thorpe* [1974]	1/20	130	170	12	900	0.25	13%
Seneca Lake	*Hunkins and Fliegel* [1973]	1/16	60	85	10	400	0.3	18%
Kootenay Lake	*Stevens et al.* [1996]	1/20	90	125	10	500	0.2	10%
Lake Biwa	*Saggio and Imberger*, [1998]	1/20	50	70	15	400	0.3	18%
	Hayami et al. [1996]				25	700	0.5	25%

Here s is the slope, h is the depth to the center of the thermocline, H is the total depth, a is the wave amplitude, and L_W is the wave length as defined in equation (1). The mixing efficiency R_f is estimated from Figure 10.

colored blue has spread some 70 cm away from its initial injection site by the end of the process (for $t > 4$ min). This provides a transport path whereby material close to the slope bottom can be swept far offshore in the deep water region.

It is important to bear in mind that the mixing efficiencies quoted above for the field sites listed in Table 2 are for individual events. The generation of internal solitary waves is a quite regular feature at many sites, such as those generated by either the interaction of the internal tide with the shelf break [e.g., *Sandstrom and Elliott*, 1984; *Holloway*, 1987] or wind events in long narrow lakes. Thus, even if the mixing efficiency is low for particular events, the regular nature of the breaking event implies that this process can be of considerable importance to mixing and transport of benthic materials over long periods of time.

Acknowledgments. This work was sponsored by Direction de la Recherche et de la Technologie (DGA) under contract 93.811.00.080 and the Australian Research Council. Bill Deugd helped in constructing the experimental facilities, and many people within the Centre for Water Research provided helpful comments. Thanks are also due to David Horn, Eric Barthélemy, and two anonymous reviewers, whose constructive criticisms helped to considerably improve the paper.

References

Apel, J. R., J. R. Holbrook, A. K. Liu, and J. J. Tsai, The Sulu Sea internal soliton experiment, *J. Phys. Oceanogr.*, *15*(12), 1665-1651, 1985.

Bogucki, D., and C. Garrett, A simple model for the shear-induced decay of an internal solitary wave, *J. Phys. Oceanogr.*, *23*(8), 1767-1776, 1993.

De Silva, I. P. D., J. Imberger, and G. N. Ivey, Localised mixing due to a breaking internal wave ray at a sloping bed, *J. Fluid Mech.*, *350*, 1-27, 1997.

Hayami, Y., T. Fujiwara, and M. Kumagai, Internal surge in Lake Biwa induced by strong winds of a typhoon, *Jpn. J. Limnol.*, *57*(4(2)), 425-444, 1996.

Helfrich, K. R., Internal solitary wave breaking and run-up on a uniform slope, *J. Fluid Mech.*, *243*, 133-154, 1992.

Holloway, P. E., Internal hydraulic jumps and solitons at a shelf-break region on the Australian North West Shelf, *J. Geophys. Res.*, *92*(C5), 5405-5416, 1987.

Hunkins, K., and M. Fliegel, Internal undular surges in Seneca Lake: A natural occurrence of solitons, *J. Geophys. Res.*, *78*(3), 539-548, 1973.

Imberger, J., Flux paths in a stratified lake· A review, in *Physical processes in lakes and oceans*, pp.1-18., J. Imberger (editor), AGU Press, 1998.

Ivey, G. N., and R. I. Nokes, Mixing driven by the breaking of internal waves against sloping boundaries, *J. Fluid Mech.*, *204*, 479-500, 1989.

Kao, T. W., F.-S. Pan, and D. Renouard, Internal solitons on the pycnocline: Generation, propagation, and shoaling and breaking over a slope, *J. Fluid Mech.*, *159*, 19-53, 1985.

Knickerbocker, C. J., and A. C. Newell, Shelves and the Korteweg-de Vries equation, *J. Fluid Mech.*, *98*, 803-818, 1980.

Koop, C. G., and G. Butler, An investigation of internal solitary waves in a two-fluid system, *J. Fluid Mech.*, *112*, 225-251, 1981.

Lamb, K. G., Numerical experiments of internal wave generation by strong tidal flow across a finite amplitude bank edge, *J. Geophys. Res.*, *99*(1), 843-864, 1994.

Leone, C., H. Segur, and J. L. Hammack, The viscous decay of long internal solitary waves, *Phys. Fluids*, *25*, 942-944, 1982.

Maurer, J., K. Hutter, and S. Diebels, Viscous effects in internal waves of two-layered fluids with variable depth, *Eur. J. Mech., B/Fluids*, *15*(4), 445-470, 1996.

Michallet, H., and E. Barthélemy, Experimental study of interfacial solitary waves, *J. Fluid Mech.*, *366*, 159-177, 1998.

Ostrovsky, L. A., and Y. A. Stepanyants, Do internal solitons exist in the ocean?, *Rev. Geophys.*, *27*(3), 293-310, 1989.

Pearson, H. J., and P. F. Linden, The final stage of decay of turbulence in a stably stratified fluid, *J. Fluid Mech.*, *134*, 195-203, 1983.

Saggio, A., and J. Imberger, Internal wave weather in a stratified lake, *Limnol. Oceanogr.*, *43*, 1780-1795, 1998.

Sandstrom, H., and J. A. Elliott, Internal tide and solitons on the Scotian shelf: A nutrient pump at work, *J. Geophys. Res.*, *89*(4), 6415-6426, 1984.

Stevens, C. L., and M. J. Coates, Applications of a maximised cross-correlation technique for resolving velocity fields in laboratory experiments, *IAHR J. Hydraul. Res.*, *32*, 195-212, 1994.

Stevens, C., G. Lawrence, P. Hamblin, and E. Carmack, Wind forcing of internal waves in a long narrow stratified lake, *Dyn. Atmosph. and Oceans*, *24*, 41-50, 1996.

Taylor, J. R., Turbulence and mixing in the boundary layer generated by shoaling internal waves, *Dyn. Atmosph. and Oceans*, *19*, 233-258, 1993.

Teoh, S. G., G. N. Ivey, and J. Imberger, Laboratory study of the interaction between two internal wave rays, *J. Fluid Mech.*, *336*, 91-122, 1997.

Thorpe, S. A., Near-resonant forcing in a shallow two-layer fluid: A model for the internal surge in Loch Ness?, *J. Fluid Mech.*, *63*, 509-527, 1974.

Wallace, B. C., and D. L. Wilkinson, Run-up of internal waves on a gentle slope in a two-layered system, *J. Fluid Mech.*, *191*, 419-442, 1988.

Wessels, F., and K. Hutter, Interaction of internal waves with a topographic sill in a two-layered fluid, *J. Phys. Oceanogr.*, *26*(1), 5-20, 1996.

Wood, I. R., and J. E. Simpson, Jumps in layered miscible fluids, *J. Fluid Mech.*, *140*, 329-342, 1984.

H. Michallet, Laboratoire des Ecoulements Géophysiques et Industriels, B.P. 53, 38041 Grenoble Cedex 9, France. (e-mail: michalle@hmg.inpg.fr)

G. N. Ivey, Centre for Water Research, University of Western Australia, Nedlands 6907, Australia. (e-mail: ivey@cwr.uwa.edu.au)

(Received March 25, 1998; revised October 15, 1998; accepted December 14,1998.)